

LIO-GVM: an Accurate, Tightly-Coupled Lidar-Inertial Odometry with Gaussian Voxel Map

Xingyu Ji¹, ShengHai Yuan¹, Pengyu Yin¹, Lihua Xie¹

Abstract—This letter presents an accurate and robust Lidar Inertial Odometry framework. We fuse LiDAR scans with IMU data using a tightly-coupled iterative error state Kalman filter for robust and fast localization. To achieve robust correspondence matching, we represent the points as a set of Gaussian distributions and evaluate the divergence in variance for outlier rejection. Based on the fitted distributions, a new residual metric is proposed for the filter-based Lidar inertial odometry, which demonstrates an improvement from merely quantifying distance to incorporating variance disparity, further enriching the comprehensiveness and accuracy of the residual metric. Due to the strategic design of the residual metric, we propose a simple yet effective voxel-solely mapping scheme, which only necessities the maintenance of one centroid and one covariance matrix for each voxel. Experiments on different datasets demonstrate the robustness and accuracy of our framework for various data inputs and environments. To the benefit of the robotics society, we open source the code at https://github.com/Ji1Xingyu/llo_gvm.

Index Terms—LiDAR inertial odometry, SLAM, voxel map, distribution

I. INTRODUCTION

THE vital requirement for an autonomous robot is to estimate its ego-motion and build a map of the environment without prior knowledge, which is widely known as Simultaneous Localization and Mapping (SLAM). In particular, the light detection and ranging (LiDAR) sensor is commonly employed for performing SLAM because of its ability to provide light-invariant and accurate range measurements. However, the LiDAR-only SLAM system may fail in degenerate scenarios (few constraints for optimization) or high-speed applications (motion distortion in the cloud). For complementary, researchers combine IMU with LiDAR [1]–[8] to form a LiDAR Inertial Odometry (LIO), as IMU can provide accurate short-term motion information and is insensitive to surroundings, thus can provide an initial pose guess and compensate for the distortion of LiDAR. Filter-based LIO [6]–[10] has been investigated in the recent few years due to its temporal and computational efficiency. The performance of a filter-based LIO system is dominated by two parts: the front end for state estimation and the mapping module for map maintenance.

The front end of a LIO system usually consists of four steps: state prediction using IMU, correspondence matching,

*This work is supported by any National Research Foundation, Singapore under its Medium Sized Center for Advanced Robotics Technology Innovation.

¹ Authors are with the Centre for Advanced Robotics Technology Innovation (CARTIN), School of Electrical and Electronic Engineering, Nanyang Technological University, Singapore. {xingyu001, shyuan, pengyu001, elhxie}@ntu.edu.sg

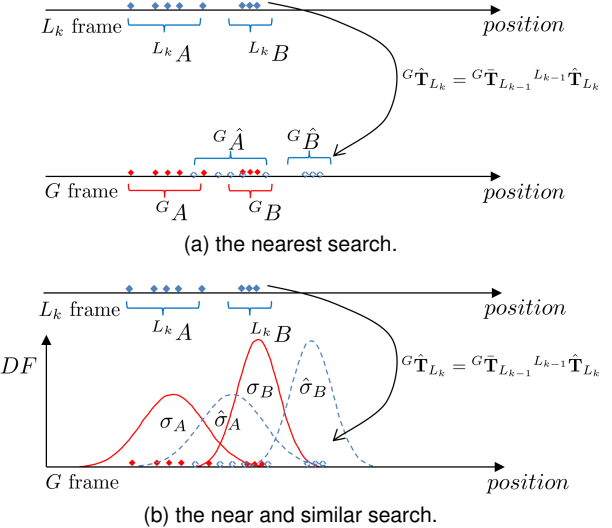


Fig. 1. Comparison of different search schemes. The blue and red points denote the point in current scan and target map respectively. The nearest search may encounter the mismatch problem, while the near and similar search can reject the pairs with large disparity in variance.

residual formulation, and state estimation. For correspondence matching, the common assumption of these filter-based LIO systems is that the point in the current scan can be approximately projected to the correct feature in the target map. This projection is dominated by the summation of historical state estimations and the state prediction using IMU. However, the accumulation of localization drifts in long-term odometry is inevitable; Simultaneously, the presence of spike noise (a severe issue in IMU, especially for the low-cost ones) leads to inaccuracies in the IMU pose guess. Thus, the assumption would be broken as shown in Fig. 1. To cope with these issues, we represent the points in both the source and target cloud as a set of Gaussian probability distributions [11]–[13] and evaluate the matched correspondences by the disparity in variance. Moreover, based on the distribution assumption, we propose a new residual metric for filter-based LIO, which allows it to assess not just the distance but also the divergence in variance. The new formula quantifies both the distance and variance disparity, further enriching the comprehensiveness and accuracy of the residual metric.

For the maintenance of the built map, k-d tree (and its variant) [14] is adopted for many systems [8]–[10] in the mapping module, as it can provide strict K nearest neighbor (k-NN) search for the correspondence matching. Some systems opt to embed a supplemental data structure (k-d tree, Hilbert Curve, etc.) within voxels to form a hierarchical structure

[6], [7], which leverages the rapid operation capabilities of voxels while also facilitating points management. Instead of storing all the raw points, we propose an incremental voxel map without any additional structures, which only maintains a centroid and covariance matrix for each voxel. The idea of this simple map scheme is inspired by the following aspects: 1) Due to the strategic design of the residual metric, the map module only necessitates the maintenance of the centroid and covariance matrix for each distribution instead of the raw points. Similar to VGICP [13], we aggregate all the distributions within a voxel (multi-point distributions to a single-voxel distribution) to estimate the distribution for the voxel robustly. Thus, we can only maintain one centroid and one covariance matrix for each voxel. 2) The strict k-NN search is unnecessary for the residual formulation since we can access the voxel in the target map where the source point occupies in. Moreover, we can evaluate the adjacent voxels by the variance divergence. 3). The time complexity for the delete, insert, and query operation of voxels (implemented by a hash table) is $\mathcal{O}(1)$, which is considerably faster than the k-d tree.

In conclusion, we implement the proposed residual metric and mapping scheme to a filter-based LIO system denoted as LIO-GVM. The contributions can be summarized as follows:

- We propose a new residual metric for filter-based LIO, which can reject mismatched correspondences as well as improve accuracy. The metric demonstrates an improvement from merely quantifying distance to incorporating variance disparity, further enriching the comprehensiveness and accuracy of the residual formulation.
- We propose a simple yet efficient map scheme in which the voxel map only necessitates the maintenance of the centroid and covariance matrix for each voxel. Due to the strategic design of the residual metric, the map module can achieve fast operation while maintaining the accuracy of state estimation.
- We implement the two key techniques into a filter-based LIO system and evaluate its efficiency through various experiments. To the benefit of the robotics community, our implementation code is open-source at https://github.com/Ji1Xingyu/lio_gvm.

II. RELATED WORKS

The SLAM problem was formulated as a state estimation problem in the early state, e.g., ESKF [15] and RBPF [16]. Many previous studies have thoroughly discussed the advantages and disadvantages of EKF [17], [18]. For example, EKF is real-time and fast, but its Markov property makes it hard to tackle long-time associations like large-scale loop closing. From the optimization perspective, EKF can also be regarded as a single-time, non-iterating factor graph with three factors (the prior, the motion, and the observation) that immediately marginalizes the previous state [19]. In LO or LIO algorithms, EKF is a prevalent backend estimator choice since the lidar point clouds are usually accurate enough to build a local map [20]. The performance of a LIO system is dominated by two factors: point cloud registration and map scheme.

TABLE I
NOTATIONS OF THIS LETTER

Notation	Explanation
G, I, L	The Global, IMU, and LiDAR frame
t_k	The end time of the k_{th} LiDAR scan
τ_i	The sample time of i_{th} IMU input, N.B. $\tau_i \in [t_{k-1}, t_k]$
${}^G\mathbf{T}_I$	The transformation matrix of I w.r.t. G
${}^G\mathbf{R}_I, {}^G\mathbf{p}_I$	The rotation matrix and translation vector of I w.r.t. G
${}^{L_k}\mathbf{p}_j$	The j_{th} point with coordinate reference to L at time t_k
${}^G\mathbf{v}_i$	The coordinate of the i_{th} voxel reference to G
${}^G\boldsymbol{\mu}_i, {}^G\mathbf{C}_i$	The centroid vector and covariance matrix of voxel at ${}^G\mathbf{v}_i$
$[\mathbf{p}]_{\times}, \mathbf{p}^T$	The skew-symmetric matrix and transpose of vector \mathbf{p}

For point cloud registration, LOAM [20] first proposes to extract the point and line features from the source and target cloud for fast registration and achieve accurate results. MULLS [21] extends the feature types and solves the optimization via a multi-metric linear least square method. Some systems only extract features in the target cloud and direct register the raw source cloud into the target map [10]. NDT [11] regards points in the target cloud as Gaussian distributions. GICP [12] fits the points in both the source and target cloud to Gaussian distributions. NDT tends to be more computationally efficient and GICP tends to be more accurate. VGICP [13] voxelized the distributions in the target map and utilizes the voxel-based association approach, which greatly increases the efficiency while retaining comparable accuracy with GICP. LiTAMIN2 [22] introduces symmetric KL-Divergence for the residual metric, which can achieve accurate pose estimation even with a small number of registered points.

For map schemes, a common method is to maintain the target map with k-d tree [20], [23], [24] for the nearest neighbor searching in the feature association phase. The conventional k-d tree needs to rebuild the entire tree for the update, which is inefficient and time-consuming. FAST-LIO2 uses the ikd-Tree [14], a dynamic k-d tree that can incrementally update the map. Faster-LIO [6] additionally introduces a pseudo-Hilbert curve inside the voxel for the acceleration of correspondence matching while maintaining accuracy.

III. PRELIMINARY

A. Notation

The important notations used in this letter are listed in Tab. I. Besides, we assume a static calibrated extrinsic matrix ${}^{L_k}\mathbf{T}_{I_k} = ({}^{L_k}\mathbf{R}_{I_k}, {}^{L_k}\mathbf{p}_{I_k})$ from IMU frame to LiDAR frame.

B. System Description

The proposed LIO-GVM is modeled as a discrete-time dynamical system sampled at the IMU rate. Its state \mathbf{x} is defined on manifold \mathcal{M} as:

$$\begin{aligned} \mathcal{M} &= SO(3) \times \mathbb{R}^{15}, \\ \mathbf{x} &\doteq [{}^G\mathbf{R}_I^T \ {}^G\mathbf{p}_I^T \ {}^G\mathbf{v}_I^T \ \mathbf{b}_\omega^T \ \mathbf{b}_a^T \ {}^G\mathbf{g}^T]^T, \end{aligned} \quad (1)$$

where ${}^G\mathbf{v}_I^T$ and ${}^G\mathbf{g}$ are the velocity of IMU and gravity vector reference to the global frame, \mathbf{b}_ω^T and \mathbf{b}_a^T are the bias vectors of gyroscope and accelerometer of the IMU.

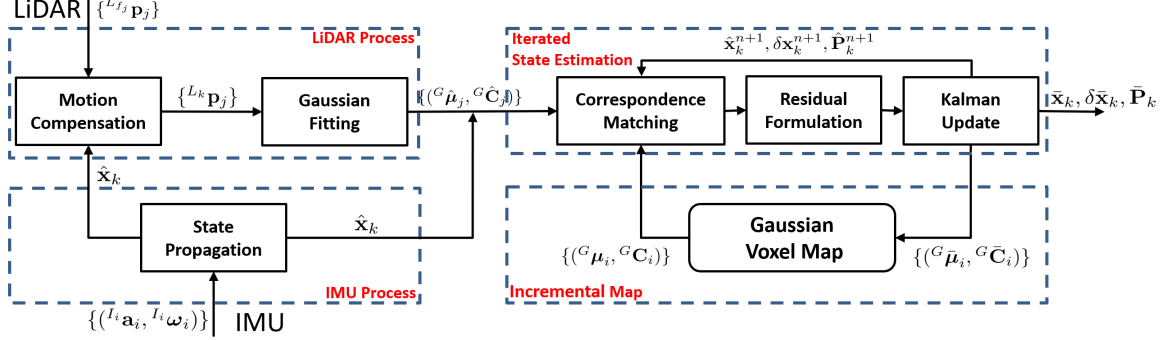


Fig. 2. System Workflow.

C. Iterative Error State Kalman Filter

In the system state \mathbf{x} defined above, the rotation matrix ${}^G\mathbf{R}_I$ are defined on $SO(3)$ in an over-parametrized way to avoid singularity, which makes it non-straightforward to estimate the system state on the manifold directly. An alternative way to estimate the state is to divide the true state \mathbf{x} into two states defined on different spaces:

$$\mathbf{x}_k = \hat{\mathbf{x}}_k \boxplus \delta \mathbf{x}_k, \quad (2)$$

$$\delta \mathbf{x}_k = [{}^G\delta \mathbf{r}_{I_k}^T \ {}^G\delta \mathbf{p}_{I_k}^T \ {}^G\delta \mathbf{v}_{I_k}^T \ \delta \mathbf{b}_{\omega_k}^T \ \delta \mathbf{b}_{\mathbf{a}_k}^T \ {}^G\delta \mathbf{g}_k^T]^T,$$

where $\delta \mathbf{x}_k \in \mathbb{R}^{18}$ is the error state, $\hat{\mathbf{x}}_k \in \mathcal{M}$ is the nominal state; \boxplus , along with \boxplus are encapsulated operators that represent a bijective mapping between the manifold \mathcal{M} and its local tangent space \mathbb{R}^{18} [25]; ${}^G\delta \mathbf{r}_{I_k}^T = {}^G\mathbf{R}_{I_k} \boxplus {}^G\hat{\mathbf{R}}_I = Log({}^G\mathbf{R}_{I_k} {}^G\hat{\mathbf{R}}_{I_k}^{-1})$ is the minimal representation of the error rotation. Consequently, we can use iterative error state Kalman filter (IESKF) to estimate the error state $\delta \mathbf{x}_k$ on Euclidean space and then project it back to the manifold using (2) for the maintenance of the true state \mathbf{x}_k . The IESKF-based LIO system generally consists of three procedures: state prediction, iterated state update, and error state reset. We will provide the details of the procedures in the context of LIO-GVM in Section IV.

IV. METHODOLOGY

The workflow of LIO-GVM is illustrated in Fig. 2. The system subscribes to IMU and LiDAR data simultaneously. All the IMU data received within the period of a LiDAR scan will be cached and propagated to the end of the scan to obtain a prediction of the state prior. Along with the estimated state and cached IMU data, LiDAR data will be fed into the LiDAR process module, where the points will be deskewed and projected to the end time of the LiDAR scan. Then each point is fitted into a Gaussian distribution with its neighbor points; thereafter, the points are projected to the global coordinate to find the corresponding voxels in the global map. Only the correspondences with similarity exceeding a certain threshold will be admitted in this procedure. The observation function will be formulated with all the accepted correspondences and fed into the IESKF state estimator for the estimation of the current state. The Incremental Map module consists of nothing

but a simple, consistently updated global voxel map. Given the estimate of the last scan: $\bar{\mathbf{x}}_{k-1}$ and $\bar{\mathbf{P}}_{k-1}$, we will detail the system workflow in turn in the following subsections.

A. IMU Process

Since the sampling period of IMU is much shorter than that of the LiDAR scan, the state prediction will be performed recursively until the end time of the current scan t_k . Recalling the state defined in (1), we have the following discrete model based on continuous kinematics equations [25]:

$$\mathbf{x}_{i+1} = \mathbf{x}_i \boxplus \mathbf{f}(\mathbf{x}_i, \mathbf{u}_i, \mathbf{w}_i), \quad (3)$$

where \mathbf{u}_i , \mathbf{w}_i , and \mathbf{f} are the system input (the IMU data), system noise, and kinematics function respectively. Please refer to Appendix A for the detailed formulations. Firstly, the mean of the nominal state $\hat{\mathbf{x}}_i$ will be predicted without considering the noise \mathbf{w}_i :

$$\hat{\mathbf{x}}_{i+1} = \hat{\mathbf{x}}_i \boxplus \mathbf{f}(\hat{\mathbf{x}}_i, \mathbf{u}_i, \mathbf{0}); \hat{\mathbf{x}}_0 = \bar{\mathbf{x}}_{k-1}. \quad (4)$$

Consequently, this will result in the accumulation of inaccuracies. To cope with the problem, \mathbf{w}_i is taken into account in the prediction of the error state $\delta \mathbf{x}_i$:

$$\delta \mathbf{x}_{i+1} \approx \mathbf{F}_{\delta \mathbf{x}} \delta \mathbf{x}_i + \mathbf{F}_{\mathbf{w}} \mathbf{w}_i; \delta \mathbf{x}_0 = \delta \bar{\mathbf{x}}_{k-1} = \mathbf{0}. \quad (5)$$

Readers may refer to [10] for the derivation and detailed formulation of $\mathbf{F}_{\delta \mathbf{x}}$ and $\mathbf{F}_{\mathbf{w}}$. In implementation, the system noise \mathbf{w}_i is considered as Gaussian white noise: $\mathcal{N}(\mathbf{0}, \mathbf{W})$. The error state $\delta \mathbf{x}_i$ is independent random vector with multivariate normal distribution: $\delta \mathbf{x}_i \sim \mathcal{N}(\mathbf{0}, \mathbf{P}_i)$. As a consequence, the predicted covariance matrix $\hat{\mathbf{P}}_{i+1}$ of $\delta \mathbf{x}_{i+1}$ can be calculated as the linear transformation:

$$\hat{\mathbf{P}}_{i+1} = \mathbf{F}_{\delta \mathbf{x}} \hat{\mathbf{P}}_i \mathbf{F}_{\delta \mathbf{x}}^T + \mathbf{F}_{\mathbf{w}} \mathbf{W} \mathbf{F}_{\mathbf{w}}^T; \hat{\mathbf{P}}_0 = \bar{\mathbf{P}}_{k-1}. \quad (6)$$

The IMU process module utilizes the state estimate from the previous scan as the initial condition and recursively predicts $\hat{\mathbf{x}}_{i+1}$, $\delta \mathbf{x}_{i+1}$ and $\hat{\mathbf{P}}_{i+1}$ till the end time of the current LiDAR scan t_k .

B. LiDAR Process

All the LiDAR points ${}^{L_j} \mathbf{p}_j$ with timestamps $\gamma_j \in [t_{k-1}, t_k]$ are cached to form a point cloud \mathcal{P}_k . ${}^{L_j} \mathbf{p}_j$ represents the point with coordinate \mathbf{p} under the LiDAR frame L_j sampling at time γ_j . For most commercial LiDAR, the points are sampled under different timestamps, which will introduce motion distortion to the cloud \mathcal{P}_k . We seek to compensate for the distortion by projecting all the points in \mathcal{P}_k to L_k , the LiDAR frame at t_k . To this end, We adopt the backward propagation proposed in [9] to obtain the relative motion between IMU frames sampled at γ_j and t_k : ${}^{I_k} \mathbf{T}_{I_j}$. The point ${}^{L_j} \mathbf{p}_j$ can thus be projected to L_k as:

$${}^{L_k} \mathbf{p}_j = {}^I \mathbf{T}_L^{-1} {}^{I_k} \mathbf{T}_{I_j} {}^I \mathbf{T}_L {}^{L_j} \mathbf{p}_j. \quad (7)$$

Moreover, a representative descriptor for the point is required for robust correspondence matching. Thus, we represent the deskewed points as a collection of Gaussian distributions. For each point ${}^{L_k} \mathbf{p}_j$, we collect its nearest y neighbors as $\{\mathbf{a}_i\}$ with $i = 0, 1, \dots, y$ and assume they are sampled from a Gaussian distribution $\mathcal{N}({}^{L_k} \boldsymbol{\mu}_j, {}^{L_k} \mathbf{C}_j)$. The maximum likelihood estimate of the distribution is:

$$\begin{aligned} {}^{L_k} \boldsymbol{\mu}_j &= \frac{1}{y} \sum_{i=0}^y \mathbf{a}_i, \\ \mathbf{A} &= [\mathbf{a}_0 - {}^{L_k} \boldsymbol{\mu}_j \quad \dots \quad \mathbf{a}_y - {}^{L_k} \boldsymbol{\mu}_j], \quad (8) \\ {}^{L_k} \mathbf{C}_j &= \frac{1}{y-1} \mathbf{A} \mathbf{A}^T. \end{aligned}$$

The Gaussian distribution assumption can be considered a good estimate of the local surface shape at a sufficiently small scale [11]. Eventually, the LiDAR process module outputs a collection of the fitted Gaussian distributions for all the points: $\{{}^{L_k} \boldsymbol{\mu}_j, {}^{L_k} \mathbf{C}_j\}$.

C. Iterated State Estimation

Upon completion of the IMU and LiDAR process, the subsequent steps for the IESKF-based LIO system involve correspondence matching, residual formulation, and Kalman update. However, the majority of existing filter-based LIO systems [6], [8], [9] typically adopt a straightforward strategy for correspondence matching, that is, matching the point ${}^{L_k} \mathbf{p}_j$ in the input LiDAR scan with its nearest feature within the target map and treating the ensuing point-to-feature distance as the residual. This strategy involves projecting ${}^{L_k} \mathbf{p}_j$ to the global frame as:

$${}^G \hat{\mathbf{p}}_j = {}^G \hat{\mathbf{T}}_{I_k} {}^I \mathbf{T}_L {}^{L_k} \mathbf{p}_j = {}^G \bar{\mathbf{T}}_{I_{k-1}} {}^{I_{k-1}} \hat{\mathbf{T}}_{I_k} {}^I \mathbf{T}_L {}^{L_k} \mathbf{p}_j. \quad (9)$$

For long-term odometry, the inevitable accumulation of localization drifts introduces errors to ${}^G \bar{\mathbf{T}}_{I_{k-1}}$; Simultaneously, the presence of spike noise, a common issue in less expensive IMUs, leads to inaccuracies in ${}^{I_{k-1}} \hat{\mathbf{T}}_{I_k}$. These factors prevent ${}^{L_k} \mathbf{p}_j$ from being projected to its exact corresponding feature, generating mismatches. Besides, matching the nearest feature in the map could be computationally intensive if the map size grows too large in long-term odometry. To cope with these issues, we propose a new residual formulation for IESKF, which can dismiss incorrectly matched correspondences while maintaining computational efficiency. The details are described in the following subsections.

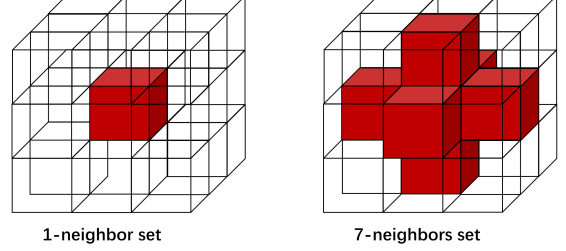


Fig. 3. Neighbor set scheme in implementation given the query voxel ${}^G \mathbf{v}_j^n$.

1) *Correspondence Matching*: Suppose the iterated state estimation module is under the n_{th} iteration; the corresponding state estimation will be $\hat{\mathbf{x}}_k^n, \delta \mathbf{x}_k^n$. We first project the fitted distributions into the global frame as:

$$\begin{aligned} {}^G \hat{\boldsymbol{\mu}}_j^n &= {}^G \hat{\mathbf{T}}_{L_k} {}^{L_k} \boldsymbol{\mu}_j, \\ {}^G \hat{\mathbf{C}}_j^n &= {}^G \hat{\mathbf{R}}_{L_k} {}^{L_k} \mathbf{C}_j {}^G \hat{\mathbf{T}}_{L_k}^T. \end{aligned} \quad (10)$$

For each projected distribution $({}^G \hat{\boldsymbol{\mu}}_j^n, {}^G \hat{\mathbf{C}}_j^n)$, we aim to find its near and similar correspondence in the global map. The global map is composed of voxels stored as a hash table: $\mathbb{Z}^3 \rightarrow \mathbb{R}^3 \times \mathbb{R}^{3 \times 3}$. The hash table maps the voxel coordinate ${}^G \mathbf{v}_i$ to its centroid ${}^G \boldsymbol{\mu}_i$ and the covariance matrix ${}^G \mathbf{C}_i$ (details of the global map is presented in Section IV-D). In order to evaluate the variance disparity, we define a scalar term derived from the squared Hellinger Distance, which we refer to as the similarity metric $s_{j,i}$:

$$s_{j,i} = \sqrt{\frac{(\det \mathbf{C}_j \det \mathbf{C}_i)^{1/2}}{\det(\mathbf{C}_j/2 + \mathbf{C}_i/2)}}. \quad (11)$$

The larger the $s_{j,i}$ is, the more similar the two distributions are. The correspondence matching procedure can now be conceptualized as follows: We first find the voxel coordinate ${}^G \mathbf{v}_j^n$ in the global map in which ${}^G \hat{\boldsymbol{\mu}}_j^n$ occupies. Then, we define a neighbor set of the occupied voxel as \mathcal{V}_j (the selection for \mathcal{V}_j in implementation is illustrated in Fig. 3. After that, we calculate the similarity $s_{j,i}$ for all the voxels in \mathcal{V}_j and discard the voxel pairs $({}^G \mathbf{v}_j^n, {}^G \mathbf{v}_i)$ with the similarity smaller than a threshold s_t . The rest voxel pairs, deemed as effective correspondences, will be utilized for the residual formulation.

2) *Residual Formulation*: Before presenting the new residual metric, it is necessary to explain the observation model and state estimate scheme for IESKF. This will provide the rationale behind the proposed residual metric. The observation function can be expressed as:

$$\begin{aligned} \mathbf{z}_k^n &= \mathbf{h}(\mathbf{x}_k) + \mathbf{v}_k \\ &= \mathbf{h}(\hat{\mathbf{x}}_k^n \boxplus \delta \mathbf{x}_k^n) + \mathbf{v}_k, \end{aligned} \quad (12)$$

where \mathbf{v}_k is the measurement noise satisfying $\mathbf{v}_k \sim n(0, \mathbf{V}_k)$, $\mathbf{h}()$ is the observation function that maps the state space to the observation space. Since the error state is quite small, we can linearize the observation at $\hat{\mathbf{x}}_k^n$:

$$\mathbf{z}_k^n \approx \mathbf{h}(\hat{\mathbf{x}}_k^n) + \mathbf{H}^n \delta \mathbf{x}_k^n + \mathbf{v}_k, \quad (13)$$

$$\mathbf{H}^n = \left. \frac{\partial \mathbf{h}(\hat{\mathbf{x}}_k^n \boxplus \delta \mathbf{x}_k^n)}{\partial \delta \mathbf{x}_k^n} \right|_{\delta \mathbf{x}_k^n = 0}, \quad (14)$$

where \mathbf{H}^n is the Jacobian matrix of $\mathbf{h}(\hat{\mathbf{x}}_k^n \boxplus \delta\mathbf{x}_k^n)$ w.r.t. $\delta\mathbf{x}_k^n$. As $\delta\mathbf{x}_k$ and $\delta\mathbf{x}_k^n$ lie in different tangent space of the manifold \mathcal{M} (the tangent space of $\hat{\mathbf{x}}_k$ and $\hat{\mathbf{x}}_k^n$ respectively), we need to project $\delta\mathbf{x}_k$ to $\delta\mathbf{x}_k^n$ in the tangent space as:

$$\delta\mathbf{x}_k = (\hat{\mathbf{x}}_k^n \boxplus \delta\mathbf{x}_k^n) \boxminus \hat{\mathbf{x}}_k = \hat{\mathbf{x}}_k^n \boxminus \hat{\mathbf{x}}_k + (\mathbf{J}^n)^{-1} \delta\mathbf{x}_k^n, \quad (15)$$

where \mathbf{J}^n is the inverse of the jacobian matrix of $(\hat{\mathbf{x}}_k^n \boxplus \delta\mathbf{x}_k^n) \boxminus \hat{\mathbf{x}}_k$ w.r.t. \mathbf{x}_k^n :

$$\mathbf{J}^n = \left(\frac{\partial (\hat{\mathbf{x}}_k^n \boxplus \delta\mathbf{x}_k^n) \boxminus \hat{\mathbf{x}}_k}{\partial \mathbf{x}_k^n} \bigg|_{\delta\mathbf{x}_k^n=0} \right)^{-1}. \quad (16)$$

Readers may refer to Appendix. A for the detailed formulation of \mathbf{J}^n . Combining (13) and (15), following the Bayesian rule, we have the maximize a posterior (MAP) problem:

$$\delta\mathbf{x}_k^n = \arg \min_{\delta\mathbf{x}_k^n} \left(\|\delta\mathbf{x}_k\|_{\mathbf{P}_k^{-1}}^2 + \|\mathbf{h}(\hat{\mathbf{x}}_k^n) + \mathbf{H}^n \delta\mathbf{x}_k^n\|_{\mathbf{V}_k^{-1}}^2 \right). \quad (17)$$

Given that the matched correspondences are Gaussian distribution pairs, we aim to design a residual metric such that the second term in (17) can represent both the distance and the variance disparity. Let's consider the weighted Mahalanobis distance presented as follow:

$$\sum_{j=0}^m (s_{j,i}^n)^2 ({}^G\hat{\mu}_j^n - {}^G\mu_i)^T (\hat{\mathbf{C}}_j^n + \mathbf{C}_i)^{-1} ({}^G\hat{\mu}_j^n - {}^G\mu_i), \quad (18)$$

where m is the number of matched correspondences. The Mahalanobis distance is weighted by the similarity of the matched correspondences, ensuring that those with higher similarity and closer distance contribute more to the estimation process, which aligns with our objective. Thus, we recover the second term of (17) back to the non-linear formulation, then equate it to (18). The resulting residual metric for $({}^G\hat{\mu}_j^n, {}^G\hat{\mathbf{C}}_j^n)$ would be:

$$\mathbf{z}_{k,j}^n = s_{j,i}^n \mathbf{D}_j^n ({}^G\hat{\mu}_j^n - {}^G\mu_i). \quad (19)$$

Please refer to Appendix. B for the derivation and detailed formulation.

3) *State Update*: The Jacobian matrix $\mathbf{H}_{k,j}^n$ of $\mathbf{z}_{k,j}^n$ w.r.t. $\delta\mathbf{x}_k^n$ is:

$$\mathbf{H}_{k,j}^n = \begin{bmatrix} -s_j \mathbf{D}_j [{}^I \mathbf{q}_j]_{\times} & s_j \mathbf{D}_j & \mathbf{0}_{3 \times 15} \end{bmatrix}. \quad (20)$$

Please refer to Appendix C for the derivation details. Suppose we have m correspondences in total, the complete Jacobian matrix is $\mathbf{H}_k^n = [\mathbf{H}_{k,0}^n \ \mathbf{H}_{k,1}^n, \dots, \mathbf{H}_{k,m}^n]$. In our implementation, we assume that the covariance matrix \mathbf{V}_k of the measurement noise is constant as \mathbf{V} . The optimal solution to the MAP problem (17) can be solved by the Kalman update [26]:

$$\begin{aligned} \mathbf{P}^n &= \mathbf{J}^n \hat{\mathbf{P}}_k (\mathbf{J}^n)^T \\ \mathbf{K}^n &= ((\mathbf{H}^n)^T \mathbf{V}_k^{-1} \mathbf{H}^n + (\mathbf{P}^n)^{-1})^{-1} (\mathbf{H}^n)^T \mathbf{V}_k^{-1} \\ \delta\mathbf{x}_k^{n+1} &= \mathbf{K}^n (\mathbf{z}_k^n - \mathbf{h}(\hat{\mathbf{x}}_k^n)) + (\mathbf{K}^n \mathbf{H}^n - \mathbf{I}) \mathbf{J}^n (\hat{\mathbf{x}}_k^n \boxminus \hat{\mathbf{x}}_k) \\ \hat{\mathbf{x}}_k^{n+1} &= \hat{\mathbf{x}}_k^n \boxplus \delta\mathbf{x}_k^{n+1}. \end{aligned} \quad (21)$$

The iteration will stop if the error state $\delta\mathbf{x}_k^{n+1}$ satisfies predetermined criteria or the count of iterations surpasses a specified threshold.

Assuming the iteration stops at n , we inject $\delta\mathbf{x}_k^{n+1}$ into $\hat{\mathbf{x}}_k^n$ to obtain the estimate of the true state $\bar{\mathbf{x}}_k$:

$$\begin{aligned} \hat{\mathbf{x}}_k^{n+1} &= \hat{\mathbf{x}}_k^n \boxplus \delta\mathbf{x}_k^{n+1}, \\ \bar{\mathbf{x}}_k &= \hat{\mathbf{x}}_k^{n+1}. \end{aligned} \quad (22)$$

For the covariance matrix, we need to project \mathbf{P}_k into the tangent space of $\bar{\mathbf{x}}_k$ as:

$$\mathbf{P}_k = \mathbf{G} \mathbf{P}^{\kappa} \mathbf{G}^T, \quad (23)$$

Readers may refer to Appendix. A for the detailed formulation. The error state can be neglected for major cases, resulting in $\mathbf{G} = \mathbf{I}|_{\delta\mathbf{x}_k=0}$; thus many implementations may ignore the state reset for simplification [10], [27]. However, for long-time odometry, adopting this procedure should reduce the accumulated drifts.

D. Incremental Global Map

Due to the strategic design of the residual formulation, the global map only necessitates the maintenance of the centroid and covariance matrix for each voxel, which is considerably efficient in terms of memory usage compared to maintaining a tree structure storing all points. Consequently, this enables an incremental update of the global map without the necessity to delete voxels from the map.

The global map is composed of voxels stored as a hash table: $\mathbb{Z}^3 \rightarrow \mathbb{R}^3 \times \mathbb{R}^{3 \times 3}$. The hash table builds a map from the voxel coordinate ${}^G\mathbf{v}_i$ to its centroid ${}^G\mu_i$ and the covariance matrix ${}^G\mathbf{C}_i$. This structure demonstrates significant efficiency in querying, achieving an optimal $\mathcal{O}(1)$ time complexity for correspondence matching.

The initialization of the global map is similar to the operation in [13]. The first frame is regarded as the global frame $G = L_0$. Each point is subsequently fitted to a Gaussian distribution as the procedure in IV-B to obtain $({}^G\hat{\mathbf{p}}_j, \mathbf{C}_j)$. Consequently, the scan is voxelized with voxel size r . Suppose we have the voxel with coordinate ${}^G\mathbf{v}_i$ encompassing a set of points $\{{}^G\mathbf{p}_m\}$, the centroid and covariance matrix will be calculated as:

$$\begin{aligned} {}^G\mu_i &= \frac{1}{M} \sum_{m=0}^M {}^G\mathbf{p}_m \\ {}^G\mathbf{C}_i &= \frac{1}{M} \sum_{m=0}^M {}^G\mathbf{C}_m. \end{aligned} \quad (24)$$

Once the current estimate $\bar{\mathbf{x}}_k$ is acquired, the current scan contributes to the global map. Since the projected Gaussian distributions have been obtained during the state estimation phase, we proceed to voxelize the current scan following (25), resulting in a temporary voxel map ${}^G\mathbf{v}_j \rightarrow (\bar{\mu}_j, \bar{\mathbf{C}}_j)$. For each voxel present in this temporary voxel map, we query its coordinate ${}^G\mathbf{v}_j$ in the global map. If the global map doesn't contain the voxel, we directly insert the voxel into the global map. This operation is time-efficient given the insert operation

for a hash table has a time complexity of $\mathcal{O}(1)$. Otherwise, the global map will be updated as:

$$\begin{aligned} {}^G\boldsymbol{\mu}_j &= \frac{M^G\boldsymbol{\mu}_j + N^G\bar{\boldsymbol{\mu}}_j}{M + N} \\ {}^G\mathbf{C}_j &= \frac{M^G\mathbf{C}_j + N^G\bar{\mathbf{C}}_j}{M + N} \\ M &= \max(M, N), \end{aligned} \quad (25)$$

where M is the recorded point number of voxel ${}^G\mathbf{v}_j$ in the global map, N is the corresponding one in the temporary voxel map.

V. EXPERIMENT

In this section, the proposed system will be evaluated in terms of accuracy, temporal efficiency, and storage efficiency. All the experiments are conducted on a laptop with a 2.3 GHz AMD Ryzen 7 6800H CPU and 16 GB RAM. We totally choose 9 sequences from two representative datasets for the evaluation. The first 5 sequences, denoted as **nc_***, are selected from Newer College dataset [28], with an OS1-64 LiDAR at a scan rate of 10Hz and a built-in 6-axis IMU sampled at 100Hz. The dataset is collected via a handheld device, transported at a moderate walking speed for a distance close to 2.2 kilometers around New College, Oxford. The area covered spans approximately $135 \times 225 \text{ m}^2$. The rest sequences are selected from MCD VIRAL dataset [29], collected by an OS1-128 LiDAR sampled at 10Hz, an Livox Mid-70 LiDAR and a VectorNav VN100 9-axis IMU sampled at 800 Hz. These sensors are mounted on an All-Terrain-Vehicle (ATV) running at high speed (30 km/h) with aggressive motion around the southern part of the Nanyang Technological University (NTU) Campus, covering around $400 \times 200 \text{ m}^2$ area. In order to evaluate the influence of IMU on the odometry accuracy, we perform experiments on different IMUs for the same sequences from MCD VIRAL dataset: **ntu_*** denoting OS1-128 LiDAR with VN100 IMU, **ntuo_*** denoting OS1-128 LiDAR with its built-in IMU. The ground truth poses for both two datasets are generated by registering each LiDAR scan to a highly accurate prior map using an ICP method.

A. Evaluation of Odometry Accuracy

The accuracy of odometry is evaluated by comparing the KITTI metric [30], the average translation error (ATE), and the average rotation error (ARE):

$$\begin{aligned} ARE &= \sum_{(i,j) \in \mathcal{F}} \text{rot}({}^G\bar{\mathbf{T}}_j {}^G\bar{\mathbf{T}}_i^{-1} {}^G\mathbf{T}_j {}^G\mathbf{T}_i^{-1}), \\ ATE &= \sum_{(i,j) \in \mathcal{F}} \| {}^G\bar{\mathbf{T}}_j {}^G\bar{\mathbf{T}}_i^{-1} {}^G\mathbf{T}_j {}^G\mathbf{T}_i^{-1} \|_2, \end{aligned} \quad (26)$$

where \mathcal{F} is a set of frames (i, j) , ${}^G\bar{\mathbf{T}}_j$ and ${}^G\mathbf{T}_j$ are the estimated and ground truth poses respectively. $\text{rot}(\cdot)$ is the rotation angle. We compare LIO-GVM with three state-of-the-art LiDAR and LiDAR-IMU odometry algorithms: DLO [31], LIO-SAM [1], and FAST-LIO2 [10]. DLO is a GICP-based LO while LIO-SAM and FAST-LIO2 are LIO systems.

It should be noted that no loop closures have been performed for all the methods.

Two variations of the proposed system LIO-GVM(w/o s) and LIO-GVM(plane), are tested for ablation study. LIO-GVM(w/o s) is implemented without the outlier rejecting correspondence matching scheme proposed in Sec. IV-C1; the similarity is still utilized in the residual formulation. LIO-GVM(plane) replaces the proposed new residual metric with the point-to-plane distance [10]. As shown in Tab. II, both LIO-GVM(w/o s) and LIO-GVM(plane) turn worse compared to the original system for all the sequences, representing that the proposed correspondence matching scheme and residual metric both contribute to the accuracy of the system. The accuracy of LIO-GVM(w/o s) tends to be much worse than LIO-GVM(plane), which is because the residual metric inherently reduces the weights for mismatches. The deterioration of the odometry is particularly evident for the **ntuo_*** sequences, in which the robot runs in an aggressive motion and is equipped with the low-cost IMU.

As illustrated in Tab. II, LIO-GVM reaches the best results for the most sequences. Note that LIO-SAM is not applicable for **ntuo_*** and **nc_*** sequences as it requires the equipment of a 9-axis IMU. For the **ntu_*** sequences, LIO-GVM achieves comparable accuracy to FAST-LIO2, outperforming the other algorithms. It is observed that LIO-GVM shows obvious superiority on **ntuo_*** sequences, which illustrates that when equipped with low-cost IMU, LIO-GVM can achieve better performance compared with other LIO systems. Similarly, the results of LIO-GVM on **nc_01** and **nc_02** demonstrate its ability to deal with accumulated drifts.

Overall, LIO-GVM has demonstrated the best performance regarding odometry accuracy, showing the effectiveness of the error-rejecting correspondence matching scheme and the distribution-based residual formulation in achieving precise location estimation across various sensor setups, especially in long-term applications or with cheaper IMUs.

B. Evaluation of Storage Efficiency

In this section, we evaluate the storage consumption of the global map generated by LIO-GVM. We employ the same parameters as those used in the experiments for evaluating the odometry accuracy. Specifically, in LIO-GVM, we have defined a custom point type using the Point Cloud Library (PCL). Each point encapsulates all the elements of $(\boldsymbol{\mu}_i, \mathbf{C}_i, M)$, comprising a total of four integer values and nine floating-point values. We save all the voxels from the global map into a .pcd (Point Cloud Data) file format. For the other systems under comparison, we configure their local map size to be 500m, ensuring coverage of all areas within the two datasets, and save all the points of the map to a .pcd file using the same function.

As illustrated in Tab. III, the map storage consumption of LIO-GVM outperforms other systems for all the sequences. This is because other systems need to ensure the downsampling filter of the map is not excessively large (usually $< 0.5\text{m}$) to preserve the geometric information of the points. In contrast, our approach, which involves maintaining merely four integer

TABLE II
EVALUATION AND COMPARISON OF ODOMETRY ACCURACY ON ALL THE SEQUENCES

	ntu_02	ntu_04	ntu_10	ntu_13	ntuo_02	ntuo_04	ntuo_10	ntuo_13	nc_01	nc_02	nc_05	nc_06	nc_07
DLO	6.46/0.43	3.65/0.11	7.65/0.51	3.98/0.20	6.46/0.43	3.75/ 0.11	7.65/0.51	3.98/0.20	4.20/0.51	4.27/0.37	3.44/0.44	1.31/0.62	1.73/0.18
LIO-SAM	7.80/0.52	3.71/0.23	9.32/0.63	3.05/0.16	- ^a	-	-	-	-	-	-	-	-
FAST-LIO2	2.09/ 0.24	2.11 /0.13	2.34 /0.15	2.89/0.11	5.64/0.80	3.51/0.23	7.32/0.41	6.79/0.50	3.23/0.37	4.15/0.43	3.13 / 0.26	0.94/0.37	1.16/ 0.15
LIO-GVM(w/o s)	2.37/0.40	2.35/0.11	3.21/0.14	2.79/0.14	5.51/0.68	4.73/0.39	6.59/0.39	4.58/0.26	3.36/0.31	4.76/0.44	3.46/0.47	1.28/0.43	1.38/0.20
LIO-GVM(plane)	8.24/0.68	6.91/0.41	8.29/0.74	5.77/0.43	9.34/0.90	7.95/0.54	10.2/0.81	8.89/0.73	6.29/0.49	6.30/0.67	4.54/0.72	2.48/0.59	3.45/0.30
LIO-GVM	1.74 /0.46	2.26 / 0.05	3.16 / 0.11	2.74 / 0.09	3.23 / 0.40	2.69 / <u>0.14</u>	4.25 / 0.27	3.60 / 0.18	2.47 / 0.26	3.20 / 0.35	<u>3.27</u> / 0.33	0.89 / 0.33	1.10 / 0.17

All the errors are represented as ATE[%]/ARE[deg/10m] (the smaller the better).

Bold value stands for the best value; underline value stands for the second best value; '-' denotes that the algorithm is not applicable.

^a The built-in IMU of OS1-128 and OS1-64 cannot provide attitude data, which is compulsory for LIO-SAM.

TABLE III
THE CONSTRUCTED MAP STORAGE ANALYSIS

	ntu_02	ntu_04	ntu_10	ntu_13	nc_01	nc_02	nc_05	nc_06	nc_07
FAST-LIO2	6.07	21.83	19.13	22.19	7.93	9.24	1.15	0.65	5.62
LIO-GVM	3.55	12.61	11.39	8.29	4.25	4.60	0.13	0.48	3.01

The map storage is analyzed by evaluating the **storage consumption [MB]** for saving the eventually constructed map.

Bold value stands for the best value.

values and nine floating-point values for each voxel yet still offering a comprehensive representation of the intra-voxel point distribution, permits us to allocate a considerably larger voxel size (commonly $> 1\text{m}$) compared to other systems. Considering that all the LiDAR scans from the 11 sequences are downsampled as a pre-processing step in all the evaluated systems, the extent of improvement in map storage of LIO-GVM compared to other systems may not exhibit significant variations for different LiDAR resolutions.

C. Evaluation of Time Consumption

In this section, we will evaluate the temporal efficiency of LIO-GVM, utilizing the same parameters as those deployed in our previous odometry evaluations for consistency. We first analyze the influence of the data structure on the mapping procedure, which involves correspondence matching and incremental updates. Given the superior performance of the ikd-Tree provided in [10] compared to other dynamic tree-based structures, our comparison will be limited to this structure. While the Gaussian fitting process does not directly participate in the mapping procedure, its time consumption is still accounted for in LIO-GVM. This is to ensure a fair comparison, as LIO-GVM requires that the points from the input scan are modeled as a Gaussian distribution, thereby indirectly involving the Gaussian fitting. We denote the data structure we use in LIO-GVM for the mapping procedure as GVM. The results are illustrated in Tab. IV. For Gaussian Fitting, ikd-Tree exhibits no time consumption, as this process is not required for this data structure. GVM significantly outperforms ikd-Tree in correspondence matching because the time complexity of k -nearest neighbors searching for ikd-Tree is $\mathcal{O}(\log(n))$, where n is the tree size; but for GVM, managed in a hash table, the corresponding time complexity is $\mathcal{O}(1)$, which is substantially faster than ikd-Tree. ikd-Tree slightly performs better in the incremental update. Nonetheless, GVM demonstrates superior performance in total map time.

In Tab. V, we illustrate the average total time consumed per scan for all the sequences. The total time we evaluated includes all the procedures: data process, pose estimate, and map update. LIO-GVM and FAST-LIO2 perform map update every time a pose is estimated. But for LIO-SAM and DLO, they run map update in another thread with the pose estimation thread; thus we only evaluate their time consumed for state estimation. Even though the mapping procedure of LIO-GVM is faster than FAST-LIO2, FAST-LIO2 achieves the shortest total time for almost all the sequences, followed by DLO, the second best. One possible reason for this could be that LIO-GVM requires more geometric information from the input scan, leading to a higher-dimensional measurement matrix. However, as illustrated in Tab. VI, the fast performance of FAST-LIO2 and DLO is at the cost of higher runtime RAM usage.

VI. CONCLUSION

In conclusion, this letter proposes an accurate filter-based LIO system denoted as LIO-GVM, which models the points as Gaussian distributions for robust correspondence matching. A key innovation that distinguishes our work from others is the proposed new residual metric for the filter-based LIO system, which marks an improvement from merely quantifying distance to incorporating variance disparity. Benefiting from the new metric, the map of LIO-GVM can be maintained in a simple yet efficient manner. We demonstrate the reliability and efficiency of LIO-GVM through extensive experiments on different datasets collected in large-scale, perceptually challenging environments. For future works, we would like to develop an adaptive voxel representation scheme for the global map, which can greatly reduce the map size as well as increase the odometry accuracy. Besides, the occupancy information is not utilized for the current work; we plan to design an efficient ray tracing method to verify the occupancy status, enabling applications such as collision detection and path planning.

TABLE IV
EVALUATION OF THE TEMPORAL EFFICIENCY IN SEQUENCES ON MAPPING PROCEDURES

	Gaussian Fitting		Correspondence Match		Incremental Update		Total Map Time	
	ikd-Tree	GVM	ikd-Tree	GVM	ikd-Tree	GVM	ikd-Tree	GVM
ntu_02	0	11.61	25.05	1.29	2.45	5.13	27.50	18.03
ntu_04	0	12.91	24.26	1.41	3.96	5.34	28.22	19.66
ntu_10	0	11.86	24.27	1.34	3.97	5.87	28.24	19.08
ntu_13	0	12.71	24.89	1.67	3.62	5.18	28.51	19.56
nc_01	0	8.10	14.36	0.69	0.78	2.97	15.14	11.76
nc_02	0	8.25	15.76	0.73	0.92	2.84	16.68	11.82
nc_05	0	7.73	12.62	0.67	0.57	2.84	13.19	11.24
nc_06	0	7.19	13.66	0.70	0.81	3.23	14.47	11.12
nc_07	0	8.99	15.67	0.62	1.11	3.18	16.78	12.79

We evaluate the **average time consumed per scan [ms]**.

Bold value stands for the best value.

TABLE V
EVALUATION OF THE TEMPORAL EFFICIENCY IN SEQUENCES ON MAPPING PROCEDURES

	ntu_02	ntu_04	ntu_10	ntu_13	nc_01	nc_02	nc_05	nc_06	nc_07
DLO(odom)	39.94	43.63	39.14	40.16	18.35	23.48	20.30	23.64	28.83
LIO-SAM(odom)	70.41	71.11	67.85	70.72	-	-	-	-	-
FAST-LIO2	37.64	39.23	38.23	38.51	19.33	21.04	17.21	19.59	20.94
LIO-GVM	47.65	46.91	49.23	47.19	26.77	28.33	28.51	27.82	30.13

The **average time consumed per scan [ms]** is evaluated.

Bold value stands for the best value;

TABLE VI
COMPARISON OF RUMTIME RAM IN SEQUENCES

	ntu_02	ntu_04	ntu_10	ntu_13	nc_01	nc_02	nc_05	nc_06	nc_07
DLO	1112	1564	1727	1389	1102	1438	513	337	809
FAST-LIO2	404	601	738	444	479	610	236	221	361
LIO-GVM	361	529	690	373	450	584	199	191	334

The eventually runtime **RAM usage [MB]** is compared.

Bold value stands for the best value;

APPENDIX

A. Supplemental Material

We provide the detail formulation of the involved matrices in the supplemental material: supplemental_material.pdf.

B. Derivation of the Proposed Residual Metric

Let's denote $({}^G\hat{\mu}_j^n - {}^G\mu_i)$ as ${}^G\tilde{\mu}$, then equate (18) with the second term in MAP problem, we'll have:

$$\begin{aligned}
 \|\mathbf{z}_k^n\|_{\mathbf{V}_k^{-1}}^2 &= \sum_{j=0}^m (s_{j,i}^n)^2 {}^G\tilde{\mu}^T (\hat{\mathbf{C}}_j^n + \mathbf{C}_i)^{-1} {}^G\tilde{\mu} \\
 &= \sum_{j=0}^m (s_{j,i}^n)^2 {}^G\tilde{\mu}^T (\mathbf{U}_j^n)^T (\Lambda_j^n)^{-1} \mathbf{U}_j^n {}^G\tilde{\mu} \\
 &= \sum_{j=0}^m (s_{j,i}^n)^2 {}^G\tilde{\mu}^T (\mathbf{U}_j^n)^T (\mathbf{Q}_j^n)^T \mathbf{V}_k^{-1} \mathbf{Q}_j^n \mathbf{U}_j^n {}^G\tilde{\mu} \\
 &= \sum_{j=0}^m s_{j,i}^n {}^G\tilde{\mu}^T (\mathbf{U}_j^n)^T (\mathbf{Q}_j^n)^T \mathbf{V}_k^{-1} s_{j,i}^n \mathbf{Q}_j^n \mathbf{U}_j^n {}^G\tilde{\mu} \\
 &= \sum_{j=0}^m (\mathbf{z}_{k,j}^n)^T \mathbf{V}_k^{-1} \mathbf{z}_{k,j}^n,
 \end{aligned} \tag{27}$$

where:

$$\begin{aligned}
 \mathbf{z}_{k,j}^n &= s_{j,i}^n \mathbf{D}_j^n ({}^G\hat{\mu}_j^n - {}^G\mu_i), \\
 \mathbf{D}_j^n &= \mathbf{Q}_j^n \mathbf{U}_j^n.
 \end{aligned} \tag{28}$$

C. Derivation of Jacobian Matrix H_j

The Jacobian matrix would be:

$$H_j^n = \frac{\partial \mathbf{z}_j(\hat{\mathbf{x}}_k \boxplus \delta \mathbf{x}_k^n, {}^L \mathbf{p}_j)}{\partial \delta \mathbf{x}_k^n} \tag{29}$$

the observation function is:

$$\mathbf{z}_j(\hat{\mathbf{x}}_k \boxplus \delta \mathbf{x}_k^n, {}^L \mathbf{p}_j) = s_{j,i}^n \mathbf{D}_j^n ({}^G\hat{\mu}_j^n - {}^G\mu_i) \tag{30}$$

The calculation of the derivative of $s_{j,i}^n \mathbf{D}_j^n$ w.r.t. $\delta \mathbf{x}_k^n$ is quite comprehensive and impractical. We assume $s_{j,i}^n \mathbf{D}_j^n$ as constant for each iteration and update its value after the iteration in the implementation. According to the experiment results, this assumption can provide enough accuracy while greatly reducing the computation load. Let's pre-process the observation function:

$$\begin{aligned}
 \mathbf{z}_j(\hat{\mathbf{x}}_k \boxplus \delta \mathbf{x}_k^n, {}^L \mathbf{p}_j) &= s_{j,i}^n \mathbf{D}_j^n \left({}^G\hat{\mathbf{p}}_{I_k} + {}^G\delta \mathbf{p}_{I_k} - {}^G\mu_j \right. \\
 &\quad \left. + {}^G\hat{\mathbf{R}}_{I_k} \text{Exp}({}^G\delta \mathbf{r}_{I_k}) ({}^I \mathbf{R}_{L_k} {}^L \mathbf{p}_j + {}^I \mathbf{p}_{L_k}) \right).
 \end{aligned} \tag{31}$$

Due to the minute transformation between two LiDAR frame, we have:

$$\text{Exp}({}^G\delta\mathbf{r}_{I_k}) \approx \mathbf{I} + [{}^G\delta\mathbf{r}_{I_k}]_{\times}. \quad (32)$$

Combine (31) and (32) we have:

$$\begin{aligned} \mathbf{z}_j(\hat{\mathbf{x}}_k \boxplus \delta\mathbf{x}_k^n, {}^L\mathbf{p}_j) &= s_j \mathbf{D}_j^n \left({}^G\hat{\mathbf{p}}_{I_k} + {}^G\delta\mathbf{p}_{I_k} - {}^G\boldsymbol{\mu}_j \right. \\ &\quad \left. + {}^G\hat{\mathbf{R}}_{I_k} {}^I\mathbf{q}_j - {}^G\hat{\mathbf{R}}_{I_k} [{}^I\mathbf{q}_j]_{\times} {}^G\delta\mathbf{r}_{I_k} \right), \end{aligned} \quad (33)$$

where ${}^I\mathbf{q}_j = {}^I\mathbf{R}_{L_k} {}^L\mathbf{p}_j + {}^I\mathbf{p}_{L_k}$. It is easy to derive the Jacobian matrix \mathbf{H}_j^n as following:

$$\mathbf{H}_j^n = \begin{bmatrix} -s_j \mathbf{D}_j^n [{}^I\mathbf{q}_j]_{\times} & s_j \mathbf{D}_j^n & \mathbf{0}_{3 \times 15} \end{bmatrix} \quad (34)$$

REFERENCES

- [1] T. Shan, B. Englot, D. Meyers, W. Wang, C. Ratti, and D. Rus, "Lio-sam: Tightly-coupled lidar inertial odometry via smoothing and mapping," in *2020 IEEE/RSJ international conference on intelligent robots and systems (IROS)*. IEEE, 2020, pp. 5135–5142.
- [2] X. Chen, P. Wu, G. Li, and T. H. Li, "Lio-ppf: Fast lidar-inertial odometry via incremental plane pre-fitting and skeleton tracking," *arXiv preprint arXiv:2302.14674*, 2023.
- [3] K. Li, M. Li, and U. D. Hanebeck, "Towards high-performance solid-state-lidar-inertial odometry and mapping," *IEEE Robotics and Automation Letters*, vol. 6, no. 3, pp. 5167–5174, 2021.
- [4] T.-M. Nguyen, D. Duberg, P. Jensfelt, S. Yuan, and L. Xie, "Slicht: Multi-input multi-scale surfel-based lidar-inertial continuous-time odometry and mapping," *IEEE Robotics and Automation Letters*, vol. 8, no. 4, pp. 2102–2109, 2023.
- [5] H. Ye, Y. Chen, and M. Liu, "Tightly coupled 3d lidar inertial odometry and mapping," in *2019 International Conference on Robotics and Automation (ICRA)*. IEEE, 2019, pp. 3144–3150.
- [6] C. Bai, T. Xiao, Y. Chen, H. Wang, F. Zhang, and X. Gao, "Faster-lio: Lightweight tightly coupled lidar-inertial odometry using parallel sparse incremental voxels," *IEEE Robotics and Automation Letters*, vol. 7, no. 2, pp. 4861–4868, 2022.
- [7] C. Yuan, W. Xu, X. Liu, X. Hong, and F. Zhang, "Efficient and probabilistic adaptive voxel mapping for accurate online lidar odometry," *IEEE Robotics and Automation Letters*, vol. 7, no. 3, pp. 8518–8525, 2022.
- [8] C. Qin, H. Ye, C. E. Pranata, J. Han, S. Zhang, and M. Liu, "Lins: A lidar-inertial state estimator for robust and efficient navigation," in *2020 IEEE international conference on robotics and automation (ICRA)*. IEEE, 2020, pp. 8899–8906.
- [9] W. Xu and F. Zhang, "Fast-lio: A fast, robust lidar-inertial odometry package by tightly-coupled iterated kalman filter," *IEEE Robotics and Automation Letters*, vol. 6, no. 2, pp. 3317–3324, 2021.
- [10] W. Xu, Y. Cai, D. He, J. Lin, and F. Zhang, "Fast-lio2: Fast direct lidar-inertial odometry," *IEEE Transactions on Robotics*, vol. 38, no. 4, pp. 2053–2073, 2022.
- [11] P. Biber and W. Straßer, "The normal distributions transform: A new approach to laser scan matching," in *Proceedings 2003 IEEE/RSJ International Conference on Intelligent Robots and Systems (IROS 2003)(Cat. No. 03CH37453)*, vol. 3. IEEE, 2003, pp. 2743–2748.
- [12] A. Segal, D. Haehnel, and S. Thrun, "Generalized-icp," in *Robotics: science and systems*, vol. 2, no. 4. Seattle, WA, 2009, p. 435.
- [13] K. Koide, M. Yokozuka, S. Oishi, and A. Banno, "Voxelized gicp for fast and accurate 3d point cloud registration," in *2021 IEEE International Conference on Robotics and Automation (ICRA)*. IEEE, 2021, pp. 11 054–11 059.
- [14] Y. Cai, W. Xu, and F. Zhang, "ikd-tree: An incremental kd tree for robotic applications," *arXiv preprint arXiv:2102.10808*, 2021.
- [15] V. Madyastha, V. Ravindra, S. Mallikarjunan, and A. Goyal, "Extended kalman filter vs. error state kalman filter for aircraft attitude estimation," in *AIAA Guidance, Navigation, and Control Conference*, 2011, p. 6615.
- [16] G. Grisetti, C. Stachniss, and W. Burgard, "Improved techniques for grid mapping with rao-blackwellized particle filters," *IEEE transactions on Robotics*, vol. 23, no. 1, pp. 34–46, 2007.
- [17] S. Huang and G. Dissanayake, "Convergence and consistency analysis for extended kalman filter based slam," *IEEE Transactions on robotics*, vol. 23, no. 5, pp. 1036–1049, 2007.
- [18] T. Bailey, J. Nieto, J. Guivant, M. Stevens, and E. Nebot, "Consistency of the ekf-slam algorithm," in *2006 IEEE/RSJ International Conference on Intelligent Robots and Systems*. IEEE, 2006, pp. 3562–3568.
- [19] W. Wen, T. Pfeifer, X. Bai, and L.-T. Hsu, "Factor graph optimization for gnss/ins integration: A comparison with the extended kalman filter," *NAVIGATION: Journal of the Institute of Navigation*, vol. 68, no. 2, pp. 315–331, 2021.
- [20] J. Zhang and S. Singh, "Loam: Lidar odometry and mapping in real-time," in *Robotics: Science and Systems*, vol. 2, no. 9. Berkeley, CA, 2014, pp. 1–9.
- [21] Y. Pan, P. Xiao, Y. He, Z. Shao, and Z. Li, "Mulls: Versatile lidar slam via multi-metric linear least square," in *2021 IEEE International Conference on Robotics and Automation (ICRA)*. IEEE, 2021, pp. 11 633–11 640.
- [22] M. Yokozuka, K. Koide, S. Oishi, and A. Banno, "Litamin2: Ultra light lidar-based slam using geometric approximation applied with kl-divergence," in *2021 IEEE International Conference on Robotics and Automation (ICRA)*. IEEE, 2021, pp. 11 619–11 625.
- [23] H. Wang, C. Wang, C.-L. Chen, and L. Xie, "F-loam: Fast lidar odometry and mapping," in *2021 IEEE/RSJ International Conference on Intelligent Robots and Systems (IROS)*. IEEE, 2021, pp. 4390–4396.
- [24] T. Shan and B. Englot, "Lego-loam: Lightweight and ground-optimized lidar odometry and mapping on variable terrain," in *2018 IEEE/RSJ International Conference on Intelligent Robots and Systems (IROS)*. IEEE, 2018, pp. 4758–4765.
- [25] C. Hertzberg, R. Wagner, U. Frese, and L. Schröder, "Integrating generic sensor fusion algorithms with sound state representations through encapsulation of manifolds," *Information Fusion*, vol. 14, no. 1, pp. 57–77, 2013.
- [26] D. He, W. Xu, and F. Zhang, "Kalman filters on differentiable manifolds," *arXiv preprint arXiv:2102.03804*, 2021.
- [27] J. Sola, "Quaternion kinematics for the error-state kalman filter," *arXiv preprint arXiv:1711.02508*, 2017.
- [28] M. Ramezani, Y. Wang, M. Camurri, D. Wisth, M. Mattamala, and M. Fallon, "The newer college dataset: Handheld lidar, inertial and vision with ground truth," in *2020 IEEE/RSJ International Conference on Intelligent Robots and Systems (IROS)*, 2020, pp. 4353–4360.
- [29] Anonymous, "Mc viral: Visual-inertial-range-lidar multi-campus dataset with continuous-time ground truth," 11 2023. [Online]. Available: <https://mcviral.github.io/>
- [30] A. Geiger, P. Lenz, and R. Urtasun, "Are we ready for autonomous driving? the kitti vision benchmark suite," in *2012 IEEE conference on computer vision and pattern recognition*. IEEE, 2012, pp. 3354–3361.
- [31] K. Chen, B. T. Lopez, A.-a. Agha-mohammadi, and A. Mehta, "Direct lidar odometry: Fast localization with dense point clouds," *IEEE Robotics and Automation Letters*, vol. 7, no. 2, pp. 2000–2007, 2022.